

Improvements for group delay fringe tracking

A.G. Basden^{1,2*} and D.F. Buscher¹

¹*Astrophysics Group, Cavendish Laboratory, Madingley Road, Cambridge CB3 0HE*

²*Astronomical Instrumentation Group, Department of Physics, Science Laboratories, University of Durham, South Road, Durham, DH1 3LE*

Released 2004 Xxxxx XX

ABSTRACT

Group delay fringe tracking using spectrally-dispersed fringes is suitable for stabilising the optical path difference in ground-based astronomical optical interferometers in low light situations. We discuss the performance of group delay tracking algorithms when the effects of atmospheric dispersion, high-frequency atmospheric temporal phase variations, non-ideal path modulation, non-ideal spectral sampling, and the detection artifacts introduced by electron-multiplying CCDs (EMCCDs) are taken into account, and we present ways in which the tracking capability can be optimised in the presence of these effects.

Key words: instrumentation: detectors – instrumentation: interferometers – techniques: interferometric – methods: statistical – methods: numerical – atmospheric effects.

1 INTRODUCTION

A stellar optical interferometer combines the light collected from a star by different telescopes to produce interference fringes. In order to see high-contrast fringes, the total optical path travelled by the light from the star to the plane of interference must be the same to within a fraction of the coherence length of the light, regardless which telescope the light beam has passed through. In ground-based interferometers the light arriving through different telescopes is subject to different and randomly-varying optical path perturbations caused by atmospheric and instrumental effects. The resulting optical path difference (OPD) is potentially many times larger than the coherence length, and so most interferometers incorporate an active method of compensating for this OPD error in real time.

The usual compensation method adopted is to sense the OPD error using some property of an interference pattern formed using light from the target star or a nearby reference star and to actuate a variable path delay in one arm of the interferometer to compensate for this error. This process is known as “fringe tracking”. Three major techniques for fringe tracking are used in interferometers worldwide: phase tracking making use of phase unwrapping methods (Shao and Staelin 1977), envelope tracking by monitoring the fringe coherence envelope (Thureau et al. 2002) and group delay fringe tracking (hereafter GDFT) by the analysis of spectrally dispersed starlight fringes

(Nisenson and Traub 1987). GDFT has the advantage over the other methods mentioned in that it is able to successfully track fringes at lower light levels (Buscher 1988; Lawson 1995). The performance of the fringe tracker at low light levels typically sets the magnitude limit of the interferometer (Buscher 1988) and so is a critical performance parameter of an interferometer system design. This paper concentrates only on the GDFT method.

Some limitations of GDFT have been studied by Lawson (1995) and references therein. However these studies have not considered a number of important problems common to real interferometers. In this paper, we quantify the effects of some of the instrumental factors that can affect the tracking capability of a system. These factors include atmospheric longitudinal dispersion, temporally-varying atmospheric phase perturbations, non-ideal spectral sampling, non-ideal optical path modulation, and the detector characteristics typical of electron-multiplying CCDs (EMCCDs). We also determine how the values of a number of parameters of the GDFT data-processing algorithm, including the window function selection, delay sampling interval and spectral channel binning factor can improve or degrade the tracking capability of a GDFT system.

The Cambridge Optical Aperture Synthesis Telescope (COAST) is being upgraded to allow fast spectro-interferometric fringe detection and group delay fringe tracking. In this paper, we use ranges of values for various system parameters which are relevant to the design of the GDFT system on the COAST interferometer, but the results we

* E-mail: abasden@mrao.cam.ac.uk

present are likely to be relevant to other interferometers worldwide.

In §2 we introduce our model for the interferometer, including the fringe detection model and the non-ideal properties of real group-delay tracking systems which we shall be considering. In §3 we describe the basic group delay tracking algorithm and the modifications to the GDFT algorithm which can be used to increase the performance of the algorithm under these non-ideal conditions. In §4 we explain the numerical simulations used to test these modifications and in §5 we provide a discussion of the results. We present our conclusions in §6.

2 INSTRUMENT MODEL

We introduce here a model of the fringe detection process which attempts to be as general as possible, so that it can be applied to different interferometers. At the same time we will restrict ourselves to values of model parameters which are appropriate to the COAST interferometer so as to give a concrete example of the model and also to simplify the discussion.

2.1 Fringe measurement

Interference patterns in optical interferometers are generally observed in the form of quasi-sinusoidal intensity variations. In different interferometers these variations may be detected spatially, for example in image-plane beam combination schemes, or temporally as exemplified by path-modulated pupil-plane schemes. We treat here only a temporally-sampled detection scheme, but most of our results will be applicable to a spatially-sampled scheme, since the mathematical treatment of these two sampling methods is similar.

We explicitly treat only single-baseline fringe-measurement schemes. Generalisation to multi-baseline schemes is straightforward in most cases: typically separate beam combiners are used to measure fringes on different baselines or an orthogonal encoding scheme is used to multiplex fringes from different baselines onto a single detector (for example by making fringes from different baselines appear at different temporal frequencies), and so analysis of the fringes on different baselines is a separable problem. We do not consider here algorithms which make use of the correlation of the information available on different baselines.

In typical temporally-sampled schemes, the optical path delay is modulated as a function of time (using for example a rapidly-moving mirror) with an approximately saw-tooth pattern, i.e. each modulation cycle consists of two segments where the OPD between the two interfering beams is made to change approximately linearly as a function of time, with the rate of change of OPD changing sign between segments. We call a single segment of this modulation pattern a ‘sweep’.

Sampling the flux emerging from the beam combiner with a single detector yields a one-dimensional sequence of intensity values in which the fringe pattern appears as a quasi-sinusoidal change of the intensity with time. If the flux is split into a number of spectral channels, for example by dispersing the light with a prism or grism onto a

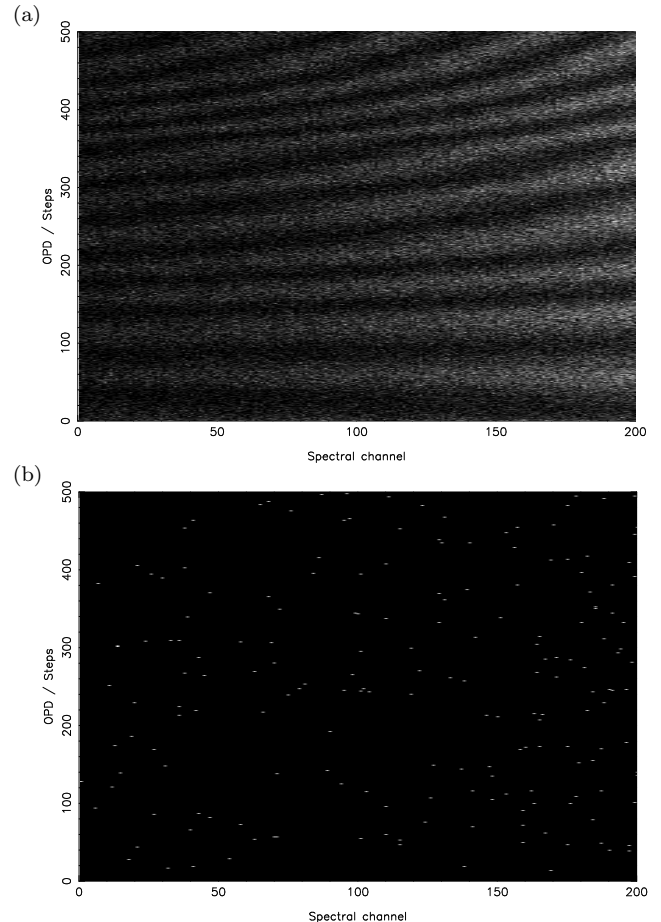


Figure 1. (a) Example of an interferometric fringe pattern showing fringes with a visibility amplitude of 0.5 and a mean light level of 20000 photons per atmospheric coherence time (2 photons per pixel), dispersed using an SF18 glass prism, and with a linear sweep. A vertical cross section of the fringe pattern will yield an quasi-sinusoidal intensity variation with the OPD (time). The total distance scanned in the OPD (y) axis is 7.6 μm , and the effect of atmospheric fluctuations can be seen to cause a change in fringe period with time. (b) A fringe identical to that in (a), but with a mean light level of only 20 photons per atmospheric coherence time (0.002 photons per pixel). The mean tracking capability for this signal level is approximately 0.75, even though no fringe is visible to the human eye.

one-dimensional array of detector pixels, then the set of intensity values measured can be represented as a discrete two-dimensional function, one coordinate being the time at which the intensity was sampled and the other being the detector pixel number. We shall call a ‘data frame’ the two-dimensional dataset obtained during the course of a single sweep. Simulated data frames at different light levels are shown in figure 1.

The intensity of an element of such a data frame (adapted from Scott (1997)) can be written as:

$$\begin{aligned} I_{jk} = & I_m(t_k, \sigma_j) + I_n(t_k, \sigma_j) \\ & + 2V_{mn}(t_k, \sigma_j) \sqrt{I_m(t_k, \sigma_j)I_n(t_k, \sigma_j)} \\ & \times \cos [2\pi\sigma_j (l_{\text{mod}}(t_k) + l_{\text{atm}}(t_k) + l_{\text{static}}) \\ & + \phi_{mn}(\sigma_j) + \theta_{mn}(\sigma_j)], \end{aligned} \quad (1)$$

where I_{jk} is the intensity measured on pixel j of the de-

tector array at time t_k , the mean wavenumber of the light falling onto pixel j is given by σ_j (i.e. $1/\lambda_j$), I_m and I_n are the intensities of the light arriving from telescopes m and n respectively, and V_{mn} represents the fringe visibility modulus. This visibility modulus takes into account the modulus of the source coherence function at wavenumber σ_j on the baseline between telescopes n and m , the effects of “smearing” of the fringes caused by fringe motion during the integration period corresponding to sample t_k , the effects of fringe smearing due to fringe phase shifts across the finite spectral bandpass falling on detector pixel j , and the effects of differential spatial aberrations (both static and randomly-varying) across the interfering wavefronts from telescopes m and n .

The fringe phase is split into OPD terms, which give rise to phase shifts which scale linearly with wavenumber, and other phase terms. The total OPD is made up of three terms: $l_{\text{mod}}(t_k)$ represents the OPD variation deliberately introduced by the path modulation system, $l_{\text{atm}}(t_k)$ represents the random OPD fluctuations due to the atmosphere and l_{static} is a “static” OPD offset which remains fixed for the duration of the sweep. The offset l_{static} includes any instrumental delay plus the mean atmospheric OPD during the sweep, and it is this quasi-static OPD which is the quantity to be estimated by our fringe-tracking algorithm.

The phase of the source coherence function at wavenumber σ_j when measured on the baseline between telescopes m and n is written as $\phi_{mn}(\sigma_j)$, and $\theta(\sigma_j)$ is a wavelength-dependent phase shift due to either instrumental effects or the wavelength dependent refractive index of the atmosphere. It is to be noted that l_{static} can be taken to include any component of the quasi-static differential phase shifts which changes linearly with wavenumber, so that $\theta(\sigma_j)$ typically represents only the non-linear component of the combined instrumental and atmospheric dispersion.

For the rest of this paper we ignore the effects of atmospheric scintillation, so that I_m and I_n are constant in time, and we further assume that $I_m(\sigma_j) = I_n(\sigma_j) = I_0(\sigma_j)$. We also assume (with little loss of generality) that the fringe intensity is sampled at equally-spaced intervals of time, i.e. t_k is a linear function of k .

2.2 Detector model

The requirements on a detector to be used for group delay fringe tracking are stringent. Since we wish to record many spectral channels simultaneously, an array of detector elements is required. One solution is to use an array of avalanche photo-diodes (APDs), as used for example at the Navy Prototype Optical Interferometer (NPOI) (Benson et al. 1998). However, this solution limits the number of spectral channels that can be used, since APDs are relatively expensive and fragile, and require fibre feeds if many are to be used, reducing the optical throughput.

Another solution is to use a charge coupled device (CCD). These devices have traditionally not been used extensively in fringe detection due to the high readout noise at the fast (MHz) pixel rates required. However, electron multiplying CCDs (EMCCDs) (Mackay et al. 2001) with sub-electron readout noise have recently been made available, and these are an attractive detector option for GDFT systems since they retain all the positive properties of conven-

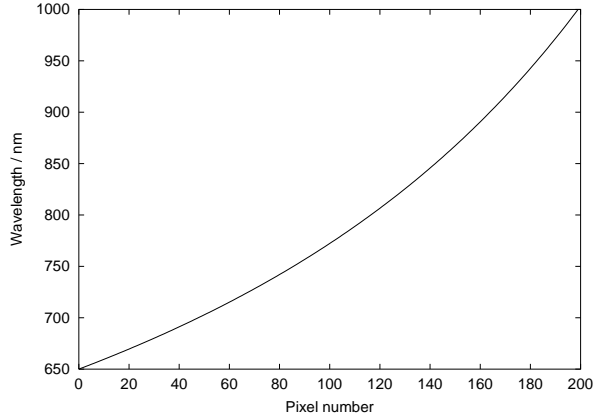


Figure 2. The dispersion relationship used to simulate dispersion from an SF18 equilateral prism, with a wavelength range of 350 nm.

tional CCDs (such as low dark current when cooled, stability, linearity). Using these devices, we can achieve a combination of high spectral resolution, high temporal resolution, high quantum efficiency and photon-counting performance, allowing fringe detection at much lower signal levels than has previously been possible.

We consider here EMCCDs as detectors for group delay fringe trackers. With sufficiently high on-chip gain and at low photon rates, EMCCDs can be considered as ideal photon-counting devices. More detailed modelling needs to take into account the additional noise in the EMCCD output signal due to the stochastic on-chip gain process, which can reduce the output signal-to-noise ratio (SNR) by up to a factor of $\sqrt{2}$ compared with the photon-noise-limited SNR. We use here the noise model described in Basden et al. (2003) and Basden (b) (2003), and the algorithms described therein, which can be used to improve the SNR of the fringe signal.

2.3 Spectrometer model

Previous analyses of GDFT algorithms have assumed that fringe pattern is spectrally dispersed such that σ_j is a linear function of j so that Discrete Fourier Transform (DFT) algorithms can be used. This ideal can be approached by using a grism and a uniformly-spaced linear array of detector pixels (Traub 1990). The GDFT system at COAST uses an SF18 glass prism for the dispersion and a linear array of EMCCD pixels, and this gives a roughly quadratic relationship between the pixel number and the wavenumber, as shown in figure 2. A second alternative would be to use a diffraction grating, which gives a spectral dispersion which is linear in wavelength, i.e. inversely proportional to wavenumber.

The wavelength range shown in figure 2 is similar to that sampled by the COAST GDFT system, i.e. 650-1000nm, sampled with 200 detector pixels.

2.4 Path modulation

On the COAST interferometer, the fringe intensity is typically sampled at a rate of 5 kHz, and a single OPD modulation sweep will last for 100 msec, i.e. 500 samples. The mod-

ulation $l_{\text{mod}}(t)$ is an approximate sawtooth in shape with a peak-to-peak path-length change of $59 \mu\text{m}$. The interference signal for a wavelength of 800nm therefore appears as a sinusoidal modulation with a fringe period of 6.56 samples.

The finite acceleration of the path modulator on COAST means that the sawtooth has “rounded edges” which last for approximately 5-10% of the sweep. Thus the fringe period will change slightly at the edges of the sweep.

2.5 Atmospheric phase perturbations

The random atmospheric fluctuations $l_{\text{atm}}(t)$ are assumed to arise from atmospheric turbulence above the telescopes following a Kolmogorov-Tatarski model and the Taylor “frozen-turbulence” hypothesis (Tatarski 1961). This model yields the temporal structure function of phase (ϕ) variations with time at a single point r on the wavefront as:

$$D_\phi(t) = \langle |\phi(r, t' + t) - \phi(r, t')|^2 \rangle = (t/t_0)^{5/3} \quad (2)$$

The atmospheric fluctuations are to a good approximation pure delay fluctuations, so the coherence time, t_0 , scales with wavelength as $\lambda^{6/5}$. On short time-scales we can assume the fluctuations at any two telescopes are uncorrelated, so that the structure function of the delay *difference* is just twice the structure function of the delay variation at a single telescope, i.e.

$$\langle |l_{\text{atm}}(t' + t) - l_{\text{atm}}(t')|^2 \rangle = \lambda_0^2 (t/t_0)^{5/3} / (2\pi^2) \quad (3)$$

where λ_0 is the wavelength at which t_0 is defined. Typical values of t_0 at COAST are around 10 msec at a wavelength of $0.8\mu\text{m}$, i.e. the sweep is approximately $10t_0$ in length.

2.6 Atmospheric longitudinal dispersion

The refractive index of air, $\eta(\sigma)$, is dependent on the wavelength of light travelling through it. If OPD compensation is not carried out in a vacuum, it is quite possible for the total path travelled in air by beams from two different telescopes to differ by many tens or hundreds of metres as shown in figure 3.

The wavelength dependence of the atmospheric refractive index introduces a phase difference between light beams which have travelled through different amounts of air. This longitudinal dispersion (relative to a reference wavenumber σ_{ref}) can be written by performing a Taylor series expansion on the expression given by Cox (1999) as

$$\theta_{mn}(\sigma_j, \sigma_{\text{ref}}) = 2\pi\sigma_j D_{mn} \left(1 - \frac{\eta(\sigma_{\text{ref}})}{\eta(\sigma_j)} \right) \quad (4)$$

$$\begin{aligned} \approx & 2\pi\sigma_j D_{\text{air}} \left[(\sigma_j^2 - \sigma_{\text{ref}}^2) \right. \\ & \times \left(1.5358 \frac{pT_s}{p_s T} + 0.346 \frac{p_w}{p_s} \right) \\ & + (\sigma_j^4 - \sigma_{\text{ref}}^4) \left(1.318 \times 10^4 \frac{pT_s}{p_s T} \right) \\ & \left. + (\sigma_j^6 - \sigma_{\text{ref}}^6) \left(1.55 \times 10^8 \frac{pT_s}{p_s T} \right) \right] \quad (5) \end{aligned}$$

where D_{air} is the net difference in air path travelled by the two beams. For an interferometer with an air delay line (such

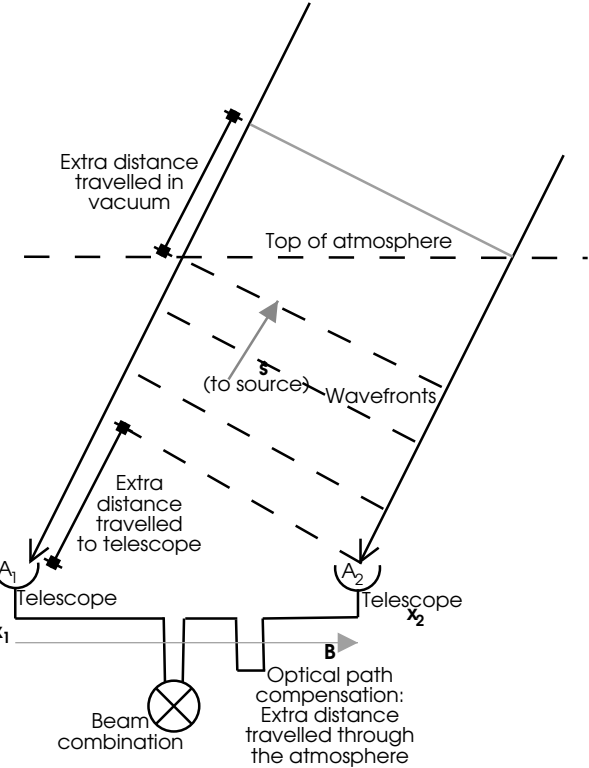


Figure 3. A demonstration of how array orientation causes light to travel different distances through the atmosphere even when the OPD is zero, if optical path compensation is not carried out in a vacuum, between two telescopes at positions x_1 and x_2 , separated by a baseline B .

as COAST) this is typically equal to D_{nm} , the projection of the baseline vector of the telescope pair n, m onto the source direction. The atmospheric pressure is p , with p_w the water vapour partial pressure and $p_s = 0.101325 \text{ MPa}$. The atmospheric temperature is T with $T_s = 288.15 \text{ K}$. We take the value of σ_{ref} to be $1/650 \text{ nm}^{-1}$, though this does not constrain the calculations in any way.

It is possible for the phase difference introduced by longitudinal dispersion to be of order several hundred radians, as shown in figure 4.

3 OPD ESTIMATION ALGORITHM

In an idealised interferometer where there is no atmospheric or instrumental dispersion, where the sweep time is much faster than the time-scale of atmospheric phase fluctuations, and where the source phase changes only slowly with wavelength, we can set $\phi_{mn}(\sigma_j), \theta_{mn}(\sigma_j) = \text{constant}$ and $l_{\text{atm}}(t) = 0$ in Eq. 1. If we were then to plot the data frame as a function of σ_j and $\sigma_j l_{\text{mod}}(t_k)$, as shown in Fig. 5, it can be seen that the measured intensity forms a sinusoidal pattern in the two-dimensional plane such that the lines of maximum and minimum intensity are sloped by an amount proportional to l_{static} . That is to say, when l_{static} is zero, the phase of the fringes is constant with wavelength and so the lines of fringe maxima lie parallel to the σ_j axis, whereas when l_{static} is non-zero, the phase changes linearly

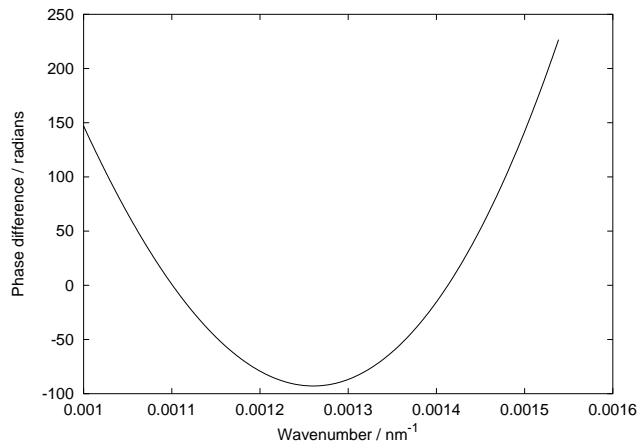


Figure 4. The effect of the longitudinal dispersion of the atmosphere for a system with air delay lines. The graph shows the residual phase shift as a function of wavelength over the wavelength range 650–1000nm for 100m of net air path difference. The best-fit group delay (i.e. linear trend of phase with wavenumber) has been removed.

with wavenumber, leading to a slope in the locus of fringe maxima.

The above argument indicates that we can determine l_{static} , the OPD offset, by measuring the rate of change of fringe phase with wavenumber σ . This process can be implemented using a two-dimensional Fourier transform in the case of an idealised interferometer, and this approach has been used by other authors (Lawson (1995) and references therein). Here we describe a more generalised two-step process which is equally applicable to an ideal or a non-ideal interferometer.

In the first step, we estimate the fringe amplitude and phase (i.e. the complex fringe amplitude) for each spectral channel. For data which is sampled at equal intervals of path delay and over an integral number of fringe cycles, this process is identical to performing a one-dimensional DFT on the time series of intensities in each wavelength channel in order to extract a single Fourier component corresponding to the fringe frequency at that wavelength.

In the second step, we choose a set of different trial OPD offsets $\{l_p\}$. For each trial OPD l_p , we shift the phase of the complex amplitude in each spectral channel by an amount $-2\pi l_p \sigma_j$ (where we note that the phase shift is a linear function of wavenumber), sum the resulting complex amplitudes over all spectral channels and take the squared modulus of the result. This squared modulus will typically be maximised when $l_p = l_{\text{static}}$. Thus the value of l_p which gives a peak in peak in the squared modulus gives an estimate of the OPD error. For data which is sampled at equal intervals of wavenumber, this second step is identical to looking for a peak in the power spectrum of the 1-dimensional complex amplitude data.

We now describe the two steps of the OPD estimation algorithm in more detail.

3.1 Determining fringe amplitude and phase

In a perfect interferometer where $l_{\text{mod}}(t_k)$ is a linear function of k during a sweep, the complex fringe amplitude can be

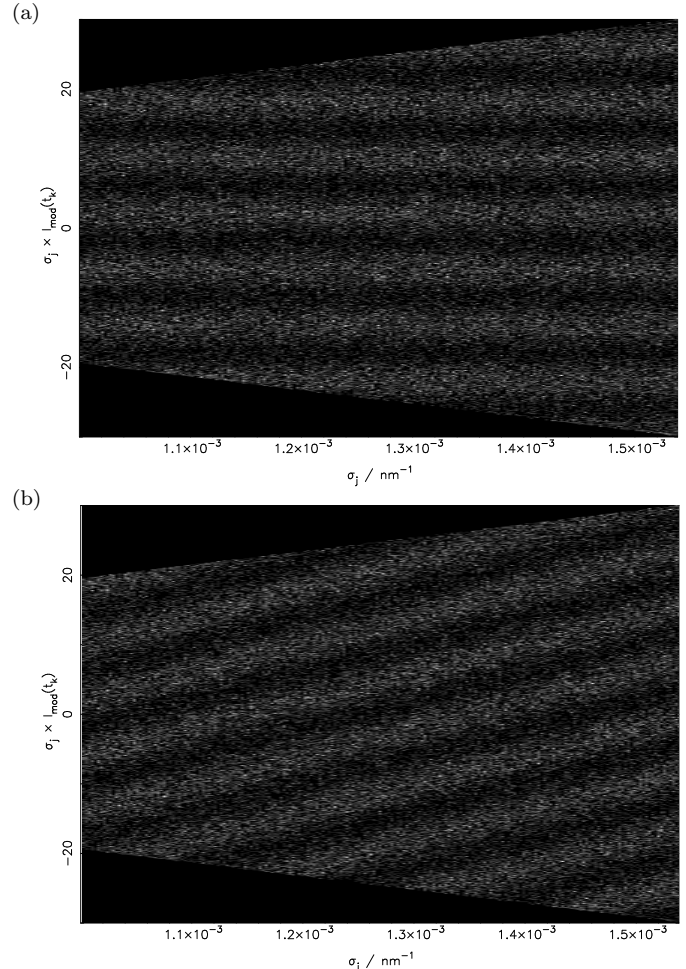


Figure 5. Fringe data with a visibility amplitude of 0.5 and mean light level of one photon per pixel plotted in a coordinate system with the y coordinate scaled by the wavenumber σ_j . The black areas outside the trapezoidal region containing fringes represent regions for which there is no data. (a) Showing the fringe pattern when the OPD is zero. (b) Showing the fringe pattern when the OPD is non-zero.

estimated using a simple DFT. We use here a modification of the DFT algorithm which can be used in cases of moderate non-linearity of the modulation waveform. An algorithm applicable over a wider range of modulation non-linearity is discussed in Thorsteinsson and Buscher (2004).

We estimate the complex fringe amplitude $F_1(\sigma_j)$ in spectral channel j using a weighted sum over the time axis of the data frame:

$$F_1(\sigma_j) = \sum_{k=1}^N W_1(t_k) \exp[-2\pi i \sigma_j l_{\text{mod}}(t_k)] \left. \frac{dt}{dl_{\text{mod}}(t)} \right|_{t_k} I_{jk} \quad (6)$$

where N is the number of intensity samples in a sweep, and $W_1(t_k)$ is a real-valued weighting function. Multiplying the data by $\exp[2\pi \sigma_j l_{\text{mod}}(t_k)] \left. \frac{dt}{dl_{\text{mod}}(t)} \right|_{t_k}$ and summing the result over k is approximately equivalent to transforming the measured intensities to a coordinate system whose independent coordinate is l_{mod} rather than t and then performing a Fourier transform. The coordinate transformation serves to

remove many of the effects of the non-linearity of l_{mod} as a function of t .

The weighting function $W_1(t_k)$ is a “window function” which typically tapers towards the edge of the sweep. The window function is introduced to reduce so-called “spectral leakage” effects, which cause components of the fringe pattern at frequencies different from the fringe frequency to contaminate the fringe signal. Typically spectral leakage becomes important when the number of fringe periods in a sweep is non-integral (see Press (1999) for further details). Since there is no single ideal windowing function we investigate some given by Press (1999) (the Welch, Bartlett, Hann, Hamming and Blackman windows), as well as the default “top-hat” window.

Note that equation 6 becomes identical to evaluating the DFT of the fringe intensity I_{jk} if we set $W_1(t_k) = 1$ and l_{mod} is a linear function of t .

3.2 Estimating the fringe power as a function of delay offset

When determining the total fringe amplitude F_2 as a function of the trial group delay l_p , we again use a generalised form of the DFT to account for a possibly non-linear variation of wavenumber with pixel index:

$$F_2(l_p) = \sum_{j=1}^M W_2(\sigma_j) \exp(-i\theta_j) \exp(-2\pi i \sigma_j l_p) \left. \frac{dx}{d\sigma} \right|_{\sigma_j} F_1(\sigma_j) \quad (7)$$

where W_2 is a window function with a similar form to that used for W_1 . The x coordinate in the differential is a continuous extension of the discrete spectral pixel coordinate j — in the typical case of a spectrometer having a uniform linear array of square detector pixels, the x coordinate is a scaled version of the spatial coordinate running along the long axis of the array, with $x = j$ at the centre of pixel j . The factor $\exp(-i\theta_j)$ serves to compensate for any wavelength-dependent phase variations due to the dispersion of the atmosphere or to instrumental effects. We typically assume that θ_j can be computed with sufficient accuracy using calibration measurements and/or atmospheric models, although we also investigate later the effect of using inaccurate atmospheric models.

We choose to evaluate F_2 over an evenly-sampled range of delays l_p such that:

$$l_p = ps/\Delta\sigma, \quad p = \{-N_p + 1, -N_p + 2, \dots, N_p\} \quad (8)$$

where $\Delta\sigma$ is the wavenumber bandpass of the spectrometer $\Delta\sigma = \sigma_1 - \sigma_M$ (the difference between the minimum and maximum wavenumbers), s is a scaling factor of order unity, and $2N_p$ trial delays are sampled. The value of s can be adjusted to sample the group more or less finely, giving a trade off between resolution and OPD range sampled for a given value of N_p . The value of N_p can be adjusted to sample a larger or smaller range of possible OPD offsets.

The resolution (smallest OPD identifiable) is given by $s/\Delta\sigma$. The range of delay space sampled is given by $N_p s/\Delta\sigma$. With unlimited computing power, N_p could be made as large as desired with s kept small, though in practice there is little point in sampling beyond the coherence length of the individual spectral channels, since the signal here is much reduced. If a constant range of delay space is

to be sampled, the number of sample points must therefore depend on the scale factor.

We next compute the square modulus of each element of F_2 , i.e. we compute $|F_2(l_p)|^2$ and look for the peak value of the modulus. The value of l_p corresponding to the peak modulus is our estimate of the OPD, hereafter the “group delay estimate”. Typical examples of the form of $|F_2(l_p)|^2$ are shown in figure 6.

More sophisticated means of determining the group delay, for example computing a centroid of the peak or making use of the phase of $F_2(l_p)$, are not considered further here. In general such techniques improve the accuracy of the group-delay estimate in high signal-to-noise-ratio (SNR) conditions, but make little difference in the low-SNR conditions which are of most interest here.

3.3 Coherent and incoherent integration

Under conditions where the time for a single path-modulation sweep is many coherence times in length, it is likely to be advantageous to break the sweep into a number of (possibly overlapping) intervals of order t_0 in length and to analyse these separately. This can be accomplished by making the window function $W_1(t_k)$ narrower than the sweep, and repeating the above analysis with the window function starting at different points along the sweep. The duration over which this window function is non-zero is hereafter called the “coherent integration time” and the values of $F_2(l_p)$ resulting from a single position of the window are termed a “coherent integration”. This integration scheme is demonstrated in Fig. 7

Under low SNR conditions we might want to make use of the information from multiple coherent integrations in order to improve the group delay estimate. Here, the primary method we use is to average together the values of $|F_2(l_p)|^2$ from multiple coherent integrations — note that this can include coherent integrations from multiple sweeps as well as from the same sweep. This averaging of the modulus squared we call “incoherent integration”.

The particular form of incoherent integration employed here uses an autoregressive filter which implements the discrete-time equivalent of a first-order low-pass filter. We assume that the coherent integration is evaluated repeatedly with the position of the coherent integration window incremented by Δt each time, and introduce the notation that $F_2(l_p, n)$ represents the result of the n th coherent integration. The output $F_3(l_p, n)$ of the autoregressive filter is given by

$$F_3(l_p, n) = a|F_2(l_p, n)|^2 + (1 - a)F_3(l_p, n - 1) \quad (9)$$

where the decay constant $0 < a \leq 1$ is defined by $a = 1 - \exp(-\Delta t/\tau)$ where τ is the time constant of the filter, i.e. the effective incoherent integration time. The position of the peak in $F_3(l_p, n)$ then gives us our group delay estimate at time $n\Delta t$.

It is possible to use *a priori* knowledge of the OPD offset (for example knowledge of the fact that offsets at closely-spaced intervals of time are likely to be correlated) to improve the estimate of the OPD (Padilla et al. 1998), but we do not make use of such algorithms here.

The estimate of the OPD error can be used to adjust the internal delays in the interferometer to so as to remove any

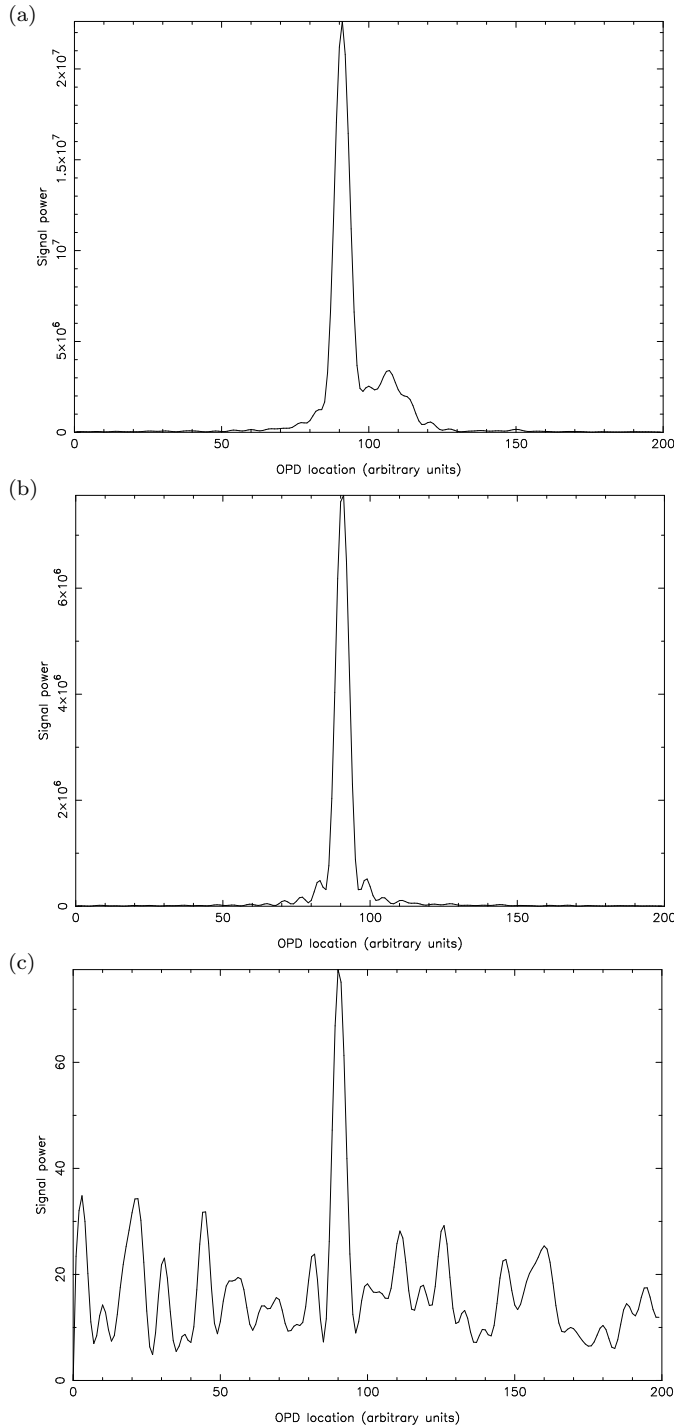


Figure 6. Examples of a typical result from the OPD locating algorithm. (a) shows the group delay signal obtained from the fringe pattern Fig. 1(a) using top-hat windowing functions, and spectral leakage is obvious. (b) shows the group delay signal obtained from a fringe pattern created using identical parameters as Fig. 1(a) using a Bartlett window during the first stage of the OPD estimation algorithm. This helps to demonstrate the effect that windowing functions have, removing spectral leakage. Plot (c) shows the signal obtained from the fringe patterns Fig. 1(b), with top-hat windowing functions. The OPD location is now obvious (with a mean tracking capability of about 0.75), even though the initial signal was very faint.

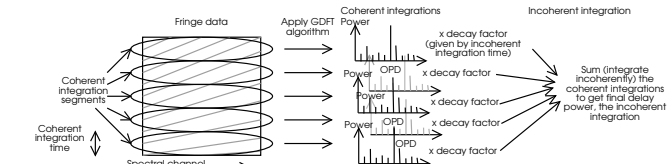


Figure 7. A schematic diagram showing how a path modulation sweep is broken into smaller lengths (coherent integrations) and the fringe tracking algorithm is applied to each of these. The resulting power is then multiplied with a decay factor and summed with the power spectrum from previous coherent integrations to give the OPD signal. The decay factor is determined by the incoherent integration time using a low-pass filter

OPD errors a closed-loop servo system. Further details are given in Benson et al. (1998). In this paper we do not consider issues relating to the performance of such a servo loop as a whole, rather we concentrate on techniques for maximising the ability to determine the OPD, i.e. maximising the fidelity of the OPD error signal.

3.4 EMCCD output processing

As discussed in section 2.2, an EMCCD can be used as a GDFT detector. However, stochastic noise is introduced into the EMCCD output signal during the on-chip gain process in addition to the photon shot noise expected from an ideal detector. We process the EMCCD output using the thresholding techniques described by Basden et al. (2003) and Basden (b) (2003) to estimate the instantaneous intensity I_{jk} . We also investigate the effect of removing this thresholding and using instead the ‘raw’ output of the EMCCD as our estimate of I_{jk} .

4 MONTE-CARLO SIMULATIONS

We investigated the effects of interferometer imperfections and processing techniques on the tracking capability of an interferometer using a series of Monte-Carlo simulations as described below.

4.1 Interferometer model selection

The first step in the simulation was to select an interferometer from the space of possible interferometer models, based on a ‘prototype’ interferometer model. The prototype model had the following characteristics:

- Wavelength range: 650-1000 nm
- Number of spectral channels: 200
- Spectral sampling: Uniform in σ (i.e. a grism)
- Path-length modulation waveform: Ideal (sawtooth)
- Peak-to-peak path-length modulation: 60 μm
- Samples per sweep: 500
- Atmospheric coherence time (t_0): 50 sample times at $\lambda = 825\text{nm}$
- Mean light level: 0.01 photons per sample per pixel (100 photons detected per t_0)
- Fringe visibility: 0.2
- Intrinsic fringe phase: 0.1
- Detector: Idealised photon-counting array

Static OPD error l_{static} : 25 μm
 Differential atmospheric path: 0 m
 Water vapour partial pressure: 0 mbar
 Temperature and pressure : $pT_s/p_s T = 1$

In the interferometer models selected, at most one parameter was changed with respect to the prototype i.e. the models selected were offset from the prototype along one “axis” in the interferometer parameter space. In this way, the effect of the varying the individual model parameters was kept separate.

4.2 Fake fringe generation

For a given interferometer model, a set of simulated spectroscopic interferometric fringes were generated. A Kolmogorov-Tatarski atmospheric model phase screen was assumed with one atmospheric phase sample for each fringe sample, and the telescope aperture size was assumed infinitesimal so that there was no phase variation across the aperture. The bandpass of each spectral channel was assumed to take the form of a top-hat function, and the finite coherence length of each spectral channel was taken into consideration by using a sinc function to envelope the fringe pattern in each spectral channel. The mean (theoretical) intensity of the fringe pattern was computed for each sample, and this intensity then “Poissonised” to produce an integer number of photons, corresponding to the theoretical intensity, with the introduction of photon noise. The mean number of Poissonian photons in each spectral channel was assumed identical to other channels unless stated otherwise. Telescope tip-tilt correction was assumed perfect.

4.3 Fringe processing

The simulated fringes were processed to obtain an estimate for the OPD using the algorithms described in section 3. The values of the parameters of the estimation algorithm were based on a prototype algorithm with the following characteristics:

Window functions W_1, W_2 : Top-hat
 Coherent integration time: 100 samples
 Offsets between successive coherent integrations Δt : 100 samples
 Incoherent integration time constant τ : 2000 samples
 Scale factor s : 0.35
 Number of trial delays $2N_p$: 200

Parameters of the data reduction algorithm were varied one at a time in the same way as the interferometer models were selected.

4.4 Performance scoring

The difference between the estimated and “true” static OPD error l_{static} was used to determine whether fringe location was successful. We quantify our results in terms of a “tracking capability” p_{track} , defined as the probability that the estimated OPD is within $1/\Delta\sigma$ of the true OPD error. If p_{track} is not unity, this means that for some fraction of the time a spurious noise peak is misidentified as being the group delay peak (since the width of the delay peak is approximately

Table 1. A table showing the effect of sweep shape on tracking capability when using fringe tracking algorithms from “previous” authors (which assume an ideal fringe pattern) and when using the algorithm presented here (“us”). A mean light level of 0.02 photons per pixel and a top-hat windowing function have been used here, and other windowing functions can lead to an improvement in tracking capability (see table 3). The poor performance of the previous tracking algorithms which assume a perfect fringe pattern means that a much higher light level would be required to achieve the same tracking capability.

OPD modulation shape	Dispersion type
Linear (Sawtooth)	0.88 ± 0.01
Sinusoidal (previous)	0.03 ± 0.01
Sinusoidal (us)	0.50 ± 0.03

$1/\Delta\sigma$). If the position of this spurious noise peak is used to send corrections to a path compensation system, then the system will tend to wander randomly away from the zero-OPD position rather than converge towards it. Thus if p_{track} falls below some threshold it is likely that the fringe signal will be lost.

The tracking capability was determined by repeating the simulated fringe generation a large number of times (typically 1000-10000) with different random realisations of the atmospheric and photon noise processes, processing the simulated fringe data and determining the relative frequency of peak misidentification.

5 RESULTS

5.1 Importance of correct coordinate transformation

Previous GDFT algorithms (Lawson 1995) assume that the dispersion is linear in σ and that the sweep modulation function is sawtoothed in shape. These algorithms then result in poor fringe tracking performance when applied to non-ideal situations typically found with real interferometers as demonstrated in tables 1 (sweep shape) and 2 (dispersion type). The low tracking capability shown here for non-ideal situations using the previous methods means that a much higher light level is required to achieve the same tracking capability that is obtained using our method presented here.

The tracking capability when using the algorithm presented here is seen to be little affected by the spectral dispersion, with table 2 comparing the tracking capability achieved with dispersion linear (in σ), dispersion expected from a SF18 equilateral prism (such as used at the COAST), and a diffraction grating with 800 lines per mm. Other non-realistic dispersions (e.g. sinusoidal) are likely to have a greater affect on tracking capability, though are not relevant for common dispersing elements such as those available at the COAST.

The sweep shape is seen to have a larger effect on tracking capability, and even when using our generalised algorithms, the tracking capability can be reduced by as much as a third when a top-hat windowing function is used.

Table 2. A table showing the effect of spectral dispersion on tracking capability when using fringe tracking algorithms from “previous” authors (which assume an ideal fringe pattern) and when using the algorithm presented here (“us”). The tracking capability is not particularly sensitive to the dispersion (for realistic dispersions on an interferometer) when our generalised algorithm is used. A mean light level of 0.02 photons per pixel has been assumed here.

Dispersion type and algorithm	Tracking capability
Linear (us and previous)	0.88 ± 0.01
Prism (previous)	0.33 ± 0.03
Prism (us)	0.87 ± 0.02
Grating (previous)	0.08 ± 0.02
Grating (us)	0.90 ± 0.01

5.1.1 Importance of the gradient weighting function

We have investigated the effect on tracking capability of the gradient function $\frac{dt}{dl_{mod}(t)} \Big|_{t_k}$, by including (the mathematically correct approach) and not including (a partial coordinate transform) this function in our OPD estimation algorithm.

When the total OPD modulation amplitude is large (with a larger change in the OPD between each sample, meaning that each fringe is sampled at only a small number of points) the lack of the gradient function does not reduce the tracking capability as shown in Fig. 8. However as the OPD modulation amplitude is reduced, the tracking capability begins to fall when the gradient function is not used, since there are then more samples taken across each fringe and so the fringe tracking algorithm is more sensitive to the change in fringe frequency as adjacent fringes are then no longer in phase. Using a gradient function then helps to reduce spectral leakage, though only has effect when the sweep or dispersion are non-linear.

We also find that the tracking capability depends on the sweep size (total distance moved during the OPD modulation cycle) with a constant distance moved between samples (i.e. taking more or less samples per sweep) when the gradient function is not used, as shown in Fig. 9. We therefore recommend that the gradient function is always included in the calculations, as this ensures that the coordinate transformation is correct, and can improve that tracking capability.

5.2 Effects of window functions

In general, the use of non-Top-hat windowing functions can improve tracking capability. When coherent integration sections overlap (e.g. the increment Δt is half the coherent integration time and so each coherent integration contains fringe signal from the preceding and following coherent integrations), windowing in the time domain can become advantageous as shown in table 3. Even though the windowing function reduces the importance of flux at the edge of the window, and hence reduces the signal, the benefit from the reduction in spectral leakage has a greater effect than the signal reduction since all parts of the sweep are now sampled close to the window maximum due to the overlapping windows used.

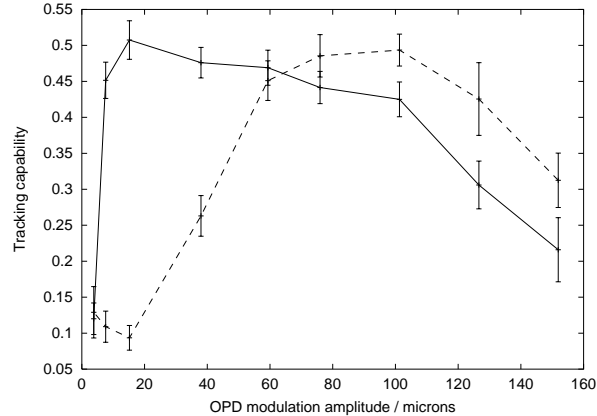


Figure 8. A plot showing how a reduction of the sweep amplitude while keeping the number of sampling points constant (all sweeps take the same amount of time regardless of length) results in more sample points across a fringe, and the gradient weighting correction ($\frac{dt}{dl_{mod}(t)} \Big|_{t_k}$) becomes more important. Here, the black trace is for a fringe analysed using a gradient weighting correction, while the dashed fringe is without, with the sweep modulation function being sinusoidal in both cases. When the total OPD modulation distance is small, the weighting correction becomes important. However, at larger OPD modulation amplitudes (60 μm is typical at the COAST), using the gradient weighting makes little difference to tracking capability. At even greater amplitudes, fringe data is under-sampled (less than two samples per fringe), and so tracking capability falls.

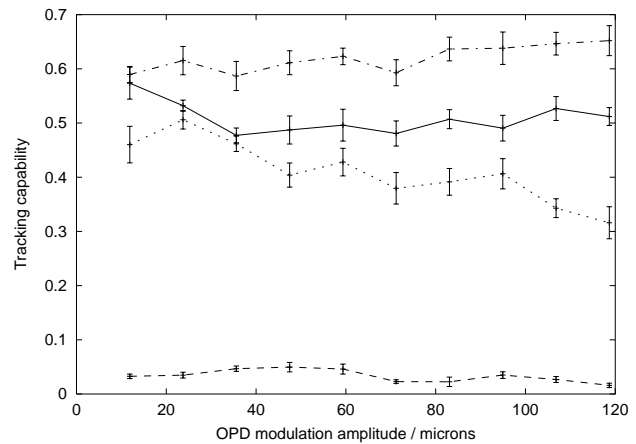


Figure 9. A graph showing how tracking capability is affected by the OPD modulation sweep size, with the number of sampling points proportional to the sweep size (so shorter sweeps take less time), but with the OPD changed by a constant amount between each sample, independent of sweep size. The dash-dotted curve shows the tracking capability for a linear sweep. The dashed curve shows the tracking capability that would be obtained using algorithms assumed by previous authors for a sinusoidal sweep. The solid curve shows fringe data with a sinusoidal sweep analysed with the algorithm presented here. The dotted curve is similar to the solid curve but does not include the gradient function in the fringe tracking algorithm. The use of a gradient function is therefore advised to avoid a reduction in tracking capability.

Table 3. A table presenting the effect of temporal windowing functions on tracking capability (values in the table) with non-overlapping and overlapping coherent integration periods, comparing linear and non-linear sweeps. It is clear that non-Top-hat windowing functions can help improve the tracking capability particularly if the sweep is not linear (sawtoothed). Uncertainties in these values are about 0.03.

Sweep Window	Overlapped		Not overlapped	
	Linear	Sinusoidal	Linear	Sinusoidal
Top hat	0.70	0.59	0.64	0.44
Welch	0.71	0.73	0.59	0.58
Bartlett	0.68	0.71	0.56	0.51
Hann	0.69	0.68	0.46	0.48
Hamming	0.72	0.69	0.53	0.56
Blackman	0.67	0.65	0.47	0.43

Table 4. A table demonstrating the effect of windowing functions on tracking capability (the values in the table) when using the OPD estimation algorithm described here with no overlap between coherent integration periods. These values were obtained using a mean light level of 100 photons per t_0 , for a linear sweep and dispersion. Errors in these tracking capability values are about 0.03 and so it is clear that the use of a top-hat windowing function gives best tracking capability.

Window type	Sweep window	Spectral window
Top hat	0.63	0.63
Welch	0.58	0.58
Bartlett	0.51	0.53
Hann	0.52	0.50
Hamming	0.56	0.49
Blackman	0.46	0.40

When coherent integrations do not overlap, i.e. the increment, Δt , of window position between each sweep segment is equal to or greater than the window size, we find that there is no advantage in using a non-top-hat windowing function in either stage of the GDFT algorithm when the sweep is linear, as shown in table 4. This is because the benefit of reducing spectral leakage by windowing is offset by the reduction in flux due to the signal reduction at the window edges. Additionally, the noise introduced by aliasing is small compared with other sources of noise (photon shot, atmospheric) when the light level is low.

We find that the use of a top-hat windowing in non-ideal situations (particularly with a non-linear sweep) can reduce the tracking capability by as much as a third as shown in tables 1 and 2. Fortunately as shown in table 3, appropriate window functions can help restore the tracking capability to that of an ideal sawtoothed modulation and so when the tracking capability is less than unity, it is advisable to use a non-top-hat windowing function. There is some evidence that a Welch window will give the best improvement in performance.

5.3 Longitudinal dispersion

If the distance travelled from a star along two separate light paths through the atmosphere before recombination differs by a large amount, then the phase difference introduced

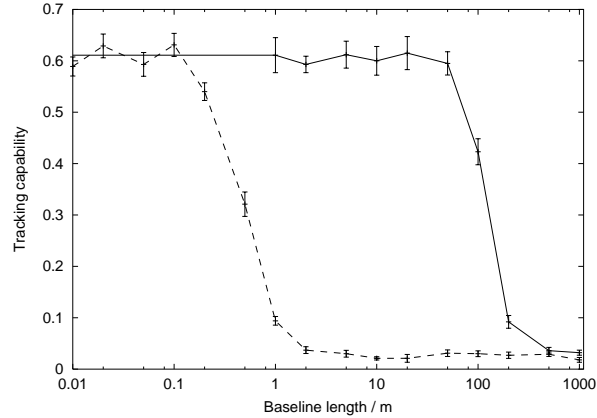


Figure 10. The effects of longitudinal dispersion and a non-zero atmospheric path difference on tracking capability when path compensation is not carried out in a vacuum. The dashed curve shows the effect of longitudinal dispersion when using previous fringe tracking algorithms (Lawson 1995) while the solid curve shows the effect when using the algorithm presented here. The improvement for longer baselines is clear.

by atmospheric longitudinal dispersion (Eq. 5) between two well spaced spectral channels will be much greater than 2π (the atmospheric dispersion is seen to introduce a phase difference of about 13 radians or 2 μm per metre of differential air path between 650 and 1000 nm). If this phase difference is not corrected for in the fringe tracking algorithms (this has been the case for most previous authors), the tracking capability will fall quickly with projected baseline length even for short baselines as shown in Fig. 10.

When a correction is made for this longitudinal dispersion phase (using Eq. 5), the tracking capability will be reduced as the phase difference approaches $2\pi l_{\text{coh}}/\lambda$ (the phase of the coherence length of the light in any given pixel), since it becomes impossible for fringes to be detected simultaneously in two well spaced wavelengths. Fig. 10 shows this effect, with tracking capability becoming reduced for atmospheric path differences greater than about 100 m, though as the light level or visibility are increased, longer baselines can still be used since the fringe signal is then clearer even though separated by large longitudinal dispersion phases. Implementing vacuum delay lines in the interferometer removes any differential longitudinal dispersion, as the total distance travelled through the atmosphere is then identical for each light beam when the OPD is zero.

5.3.1 Atmospheric uncertainties

The exact form of the longitudinal dispersion may not be known, being dependent on both the model used and the atmospheric conditions. We therefore investigate the effect of imprecise knowledge of atmospheric conditions when interpreting the results, and also investigate the effects of model dependencies. Fig. 11(a) shows the effect on tracking capability when different atmospheric conditions are used to produce fringes ($(p/T)_{\text{produce}}$) than are assumed when computing the OPD ($(p/T)_{\text{compute}}$), and this uncertainty can be characterised by the quantity

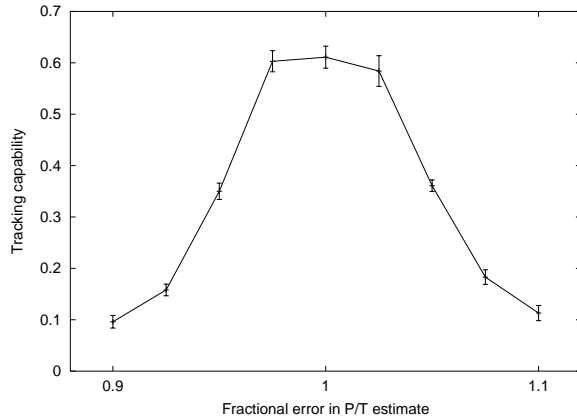


Figure 11. Simulated effect of imprecise knowledge of atmospheric temperature and pressure when fringe tracking for a projected baseline length of 10m, showing that the reduction in tracking capability is approximately Gaussian about the true value, with the width corresponding to an error of about 0.07 in pressure or temperature. This effect is due to the atmospheric longitudinal dispersion.

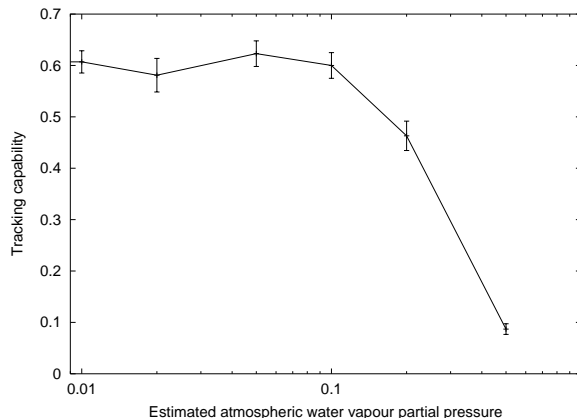


Figure 12. Simulated effect of imprecise knowledge of atmospheric water partial pressure when fringe tracking for a differential atmospheric path of 10m, showing that the reduction in tracking capability is minimal for all likely atmospheric humidities. No water vapour was assumed when producing the fringes.

$$C = \frac{(p/T)_{\text{produce}}}{(p/T)_{\text{compute}}}. \quad (10)$$

The loss in tracking capability is only small if $|1 - C| < 0.02$. This loss is found to depend on $|1 - C|$ following a Gaussian distribution with a width of about 0.07. For example, if a fringe pattern is simulated at standard temperature and pressure, and the fringe tracking algorithm computed assuming a pressure increase of one percent ($|1 - C| = 0.01$), the tracking capability is barely affected. However, if the pressure is increased by ten percent ($|1 - C| = 0.1$), the tracking capability is greatly reduced.

We also find that the tracking capability is virtually independent of the error made when estimating humidity for atmospheric conditions found on earth (Fig. 12).

We have yet to discover how effective our method will be when applied to real data, though it is likely that any model discrepancy will be small, since the atmospheric re-

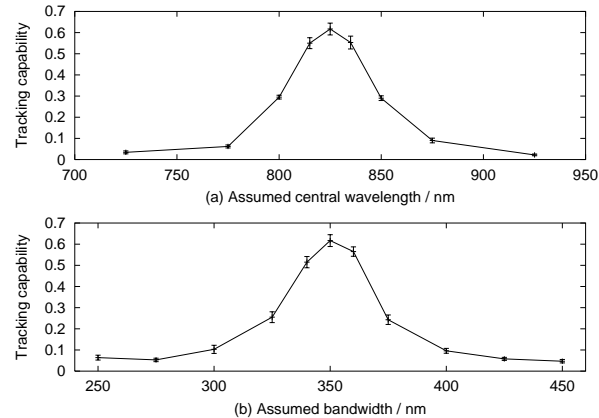


Figure 13. Plots showing the effect of an unknown wavelength-pixel relationship. In (a), we can see that it is important to be able to locate the central wavelength of the dispersed light accurately to within 10-20 nm to avoid a significant loss in tracking capability. In (b), we see that the bandwidth of the light must be estimated to within about 20 nm. In both of these plots, the true total bandwidth was 350 nm, centred at 825 nm. We find that this tolerance is independent of the dispersion (e.g. linear, prism or grating).

fractive index has been well studied. Atmospheric conditions are typically known to much better than one percent, and so it is likely that this effect will be minimal. The longitudinal phase correction does not depend on terms independent of wavelength, since this just adds a constant phase.

5.4 Pixel-wavelength relationship

We find that if the pixel-wavelength relation is not known precisely, then the tracking capability is reduced. Fig. 13 (a) shows that the centre of the spectrum should be located with about 1-2 percent accuracy (typically 5-10 pixels for a 350nm bandwidth spectrum at 820nm, assuming 256 spectral channels). Likewise, Fig. 13 (b) shows that the total bandwidth should be known to about 5 percent so that tracking capability is not significantly reduced. In practice, the wavelength-pixel relationship will be known to better than this as it can be accurately determined from the fringe frequencies, and so the effect shown here will be minimal unless misalignment occurs.

5.5 Sampling scale

The sampling scale (s) used does not affect the way the detector is read out and hence many different scales can be used each modulation half-period until the scale giving maximum tracking capability is found. As shown in Fig. 14, we find that when the sampling scale is large (> 2) or small (< 0.2), tracking capability may be reduced since there is an increase in spectral leakage. By using a small sampling size, it is possible to locate a fringe envelope maximum to within a fraction of a wavelength provided the OPD is small.

If computing power limits the number of delay space samples that can be calculated for each data frame, it may be advantageous to use a large scale factor to identify the OPD initially. The OPD can then be reduced using optical

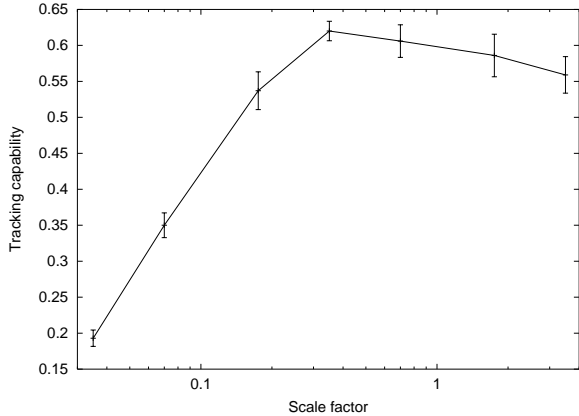


Figure 14. Showing the effect of changing the scale factor. If the scale factor is too small, the tracking capability is reduced, while if too large, the resolution to which the OPD can be specified is reduced. We see that tracking capability remains high for scale factors between 0.2-2. However, if the scale factor gets too large, we are unable to identify the OPD correctly, as our resolution is then not great enough.

path compensators, and a smaller sampling scale can then be used to refine the OPD estimation, whilst all the time calculating a constant number of delay space samples.

5.6 Coherent and incoherent integrations

It has been shown (Buscher 1988) that the optimal time over which to integrate coherently is about $1.6t_0$, allowing for a tradeoff between received energy and temporal smearing due to atmospheric perturbations. Further incoherent integration (Eq. 9) is of advantage, where frames are summed over a time-scale of typically between $20t_0$ (Lawson 1995) - $40t_0$ (Buscher 1988). There is some discrepancy between these two estimates, and so we investigate the best time-scale over which to integrate both coherently and incoherently using the sweep combination algorithm, Eq. 9.

Fig. 15 shows the simulated effect of integration time on tracking capability. Short coherent integration time-scales of about t_0 - $2t_0$ achieve the best tracking capability during a single sweep, in agreement with Buscher (1988), while using an incoherent integration time of between 20 - $50t_0$ also maximises the tracking capability.

We recommend the general use of a coherent integration time of $1.6 t_0$ and an incoherent integration time of about $30 t_0$ for general use.

5.7 Effects of intensity variation with wavelength

Intrinsic variations of source intensity with wavelength (for example due to stellar atmosphere absorption), and a change in detector quantum efficiency with wavelength mean that the mean intensity of a fringe will depend on spectral channel. For most of our calculations we assume a flat source power spectrum, with equal power produced for each spectral channel. However, we have also investigated several other models for stellar atmospheres, particularly those for cool stars, as these are commonly observed with optical stellar interferometers. We use a stellar power spectrum for both

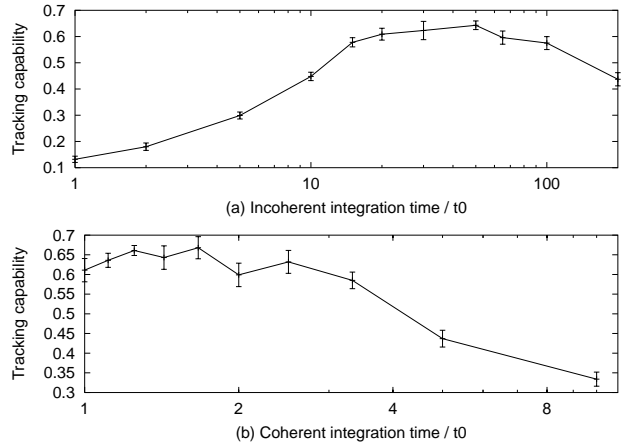


Figure 15. The effect of integration times on tracking capability. The top trace shows the effect of incoherent integration time on tracking capability, and is seen to peak between about 20 - $50t_0$. The lower trace shows the tracking capability as a function of coherent integration time, and shows that shorter integration times are favoured.

61 Cyg A and WX Cam taken from Turnshek et al. (1985). We also investigate the inclusion of a model of EMCCD quantum efficiency and find that using such spectra makes negligible difference to the fringe tracking capability, when compared with models using a constant mean flux with the same number of photons detected in the fringe. This is the case even when large absorption bands are present within the stellar spectra.

We find that for a given mean detected flux, the tracking capability does not depend on the wavelength intensity relationship for commonly occurring wavelength-intensity dependencies. The presence of large stellar atmosphere absorption bands have little effect on tracking capability.

5.8 Combination of spectral channels

At low light levels, there may only be at most a few detected photons in each spectral channel during the optical delay modulation half-period. It may therefore be tempting to combine spectral channels together, with the hope of reducing the phase error when estimating the phase of the fringe in each spectral channel.

Spectral channel combination can either be carried out before CCD readout, or afterwards in software. Pre-readout spectral channel combination has the disadvantage that once spectral channels have been combined there is no way of returning to the higher spectral resolution. Therefore, spectral combination in software is the best option if CCD readout noise is negligible, as with EMCCDs. If CCD readout noise is non-negligible or a very rapid readout is required, it may be appropriate to bin spectral channels together before readout.

Combining spectral channels will reduce the coherence length of each channel, and so if the number of spectral channels combined becomes large, there will be a reduction in tracking capability since as the coherence length approaches the OPD, it becomes more difficult to find and track fringes. We investigate the effects of combining between 1-5 spectral channels together, and find that there is a decrease in track-

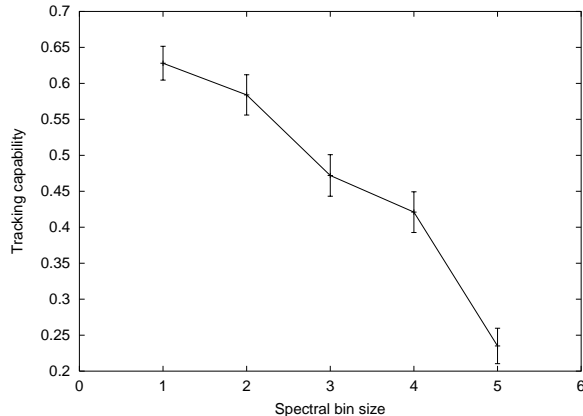


Figure 16. A graph showing how combining spectral channels by summing raw data in adjacent channels can reduce tracking capability due to smearing of fringe, and so is not recommended.

ing capability as more channels are combined (Fig. 16), due to smearing of the fringes at the edges of the modulation where the rate of change of fringe phase with wavenumber typically becomes large. This technique is therefore not recommended.

5.9 EMCCDs for group delay fringe tracking

Being array detectors, EMCCDs can be used as group delay fringe tracking detectors, since they are capable of recording a one dimensional spectrum rapidly. We model the use of an EMCCD for GDFT assuming the model given by Basden et al. (2003), with a mean on-chip gain of 6629, assuming a RMS readout noise of 50 electrons is introduced to the multiplied signal. The EMCCD output first has a noise level at 300 electrons removed, and is then treated using different thresholding strategies following Basden et al. (2003); Basden (b) (2003) (the Analogue, Digital, Uniform and Poisson Probability thresholding strategies), ignoring the effects of dark current which will be small due to the fast readout.

Fig. 17 shows the effect that the EMCCD and associated thresholding strategies have on the tracking capability of a GDFT system. If the Analogue strategy is used, twice as many photons are required to achieve the same tracking capability as that achieved with a perfect detector (independent of the light level), and this is expected due to the reduction in effective quantum efficiency due to the stochastic multiplication process (Basden et al. 2003). However, if the EMCCD output is processed appropriately, the effect of stochastic multiplication noise can be minimised at low light levels, and the fringe tracking capability can be improved as shown in these figures. At light levels greater than about two photons per pixel (Fig. 17(a)), there is little benefit in thresholding the EMCCD output, in agreement with results obtained in previous chapters. The Uniform thresholding strategy (Basden (b) 2003) appears to give the most consistent improvement in tracking capability, and at light levels less than about 0.2 photons per pixel the tracking capability is almost that of an ideal detector since the EMCCD is then operated in photon counting mode.

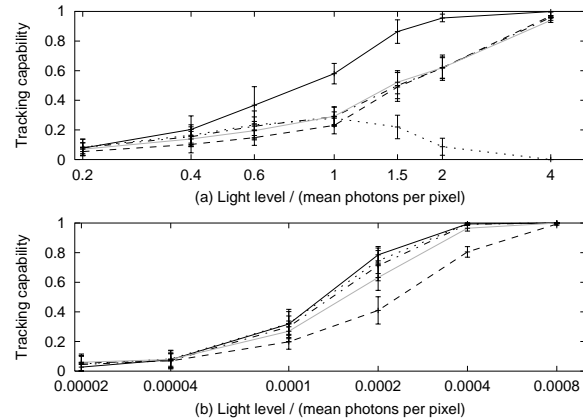


Figure 17. Simulated tracking capability when using an EMCCD as the detector for a fringe visibility of (a) 0.02 and (b) unity. The black curve represents the tracking capability for a perfect detector (Poisson noise only). The dashed curve is when using the raw output of an EMCCD, the dotted curve is when using a single threshold on the raw EMCCD output, the dot-dashed curve is when using a uniform thresholding strategy and the grey curve is when using a Poisson probability thresholding strategy. At low light levels, there is much advantage of thresholding the data. When the light level is high, typically twice as much light is required to achieve the same tracking capability with the raw output as would be needed for a perfect detector.

5.9.1 Low light levels

At low light levels (< 1 photon per pixel) the EMCCD can be operated in a photon counting mode, treating every signal above some noise level as representing one photon (Basden et al. 2003). Tracking capability is almost that of a perfect detector (Fig. 17(b)). Alternatively using the Uniform multiple thresholding strategy described by Basden (b) (2003) gives a similar tracking capability.

5.9.2 Higher light levels

At higher light levels (with the mean light level approaching or greater than one photon per pixel), coincidence losses when using a single threshold become large, since there is a significant probability that we would interpret two or more photons as being one photon. This leads to a reduction in tracking capability as demonstrated in Fig. 17(a).

Using multiple thresholds (Basden (b) 2003) can improve the tracking capability at these light levels, and although the estimated number of photons is not always correct, we do significantly better than when using a single threshold. This leads to an improvement in tracking capability, though we are still not able to track as well as an ideal detector would allow. The results in Fig. 17 show that we are still able to improve tracking capability over that achieved with the raw output for light levels up to about 2 photons per pixel.

Using the raw EMCCD output (after subtracting a noise level) gives a better result than when using a single threshold for light levels above about 1 photons per pixel. It is also not significantly worse than a multiple thresholded output mode when the light level is greater than about two photons per pixel. At these light levels, approximately twice

as much light is required to achieve a given tracking capability as would be needed using an ideal detector, which is the main disadvantage when using EMCCDs at high light levels.

5.9.3 Ideal output interpretation

These results are in agreement with those presented by Basden et al. (2003) showing that the effect of EMCCD stochastic multiplication noise can be successfully reduced at low light levels. The best approach for fringe tracking with an EMCCD is to place the EMCCD output into multiple thresholds with a threshold spacing dependent on mean gain and light level (which can be estimated for each spectral channel by averaging the received signal), as described by Basden (b) (2003). This mode allows us to track well at any light level, making most use of the information that we have. At the lowest light levels, we have a tracking capability similar to that of an ideal detector, while at higher light levels (of order one photon per pixel or more) it is not so good.

Since best results are achieved at light levels less than one photon per pixel, the EMCCD should be operated in this regime if possible, increasing the pixel rate where appropriate to reduce the signal on each pixel. At very high light levels, the EMCCD could be used in a non-amplifying mode, where the signal detected by the CCD is not amplified at all, and noise in the signal is then due to readout noise and photon Poisson noise. However, it is unlikely that spectroscopic interferometric signals will contain this amount of flux.

6 CONCLUSIONS

The maximisation of the performance of GDFT algorithms using Monte-Carlo simulation has been investigated. Previous authors (Lawson (1995) and references therein) have typically assumed ideal conditions when investigating GDFT algorithms. However, here it has been shown that when used in real situations, these algorithms may give poor performance. Investigations into the performance of a generalised GDFT algorithm has shown that the tracking capability can be improved, leading to the following conclusions:

(i) The non-linear dispersions typically resulting from prism or grating dispersion elements do not affect tracking capability significantly. When appropriate windowing functions are used, a non-sawtoothed OPD modulation will not affect the tracking capability, though this can be reduced by up to a third if a top-hat windowing function is used,

(ii) Atmospheric longitudinal dispersion can in theory be corrected for sub-kilometre baselines, though analysis of real data is needed to verify this.

(iii) Coherent integration for about $1.6t_0$ gives the largest improvement in tracking capability.

(iv) Incoherent integration times between about 20-50 t_0 lead to maximisation of the tracking capability. If longer incoherent integration times are used, the OPD signal can become smeared over several locations due to the temporal atmospheric fluctuations.

(v) Windowing functions can lead to an improvement in

tracking capability particularly when used with overlapping coherent integrations, and when the sweep function is non-ideal. When performing a transform over spectral channels, spectral windowing functions are not seen to give a significant improvement in tracking capability.

(vi) Summing adjacent spectral channels leads to a reduction in tracking capability.

(vii) Altering the sampling scale of which the delay space is sampled can be used to increase the range of OPD positions detectable, or increase the accuracy of detection.

(viii) Using an EMCCD as a photon counting detector gives the tracking capability expected from an ideal detector at light levels less than one photon per pixel. At higher light levels, up to twice as much light needs to be collected on an EMCCD to achieve the same tracking capability as an ideal detector.

REFERENCES

Baldwin J. E., Haniff C. A., 2001, *Phil. Trans. A*, 360, 969-986
 Basden A. G., Haniff C. A. and Mackay C. D., *MNRAS* 345, p. 985-991
 Basden A. G. and Haniff C. A., 2003, *MNRAS* 347, p. 1187-1197.
 Benson J. A., Mozurkewich D., Jefferies S. M., 1998, *Proc. SPIE* 3350, p. 492 *Astronomical interferometry*
 Buscher D. F., 1988, PhD thesis, University of Cambridge
 Cox A. N., *Allens Astrophysical Quantities*, 4th edn, AIP Press
 Thorsteinsson H., Buscher, D. F., 2004, "General fringe decomposition and bias correction in optical interferometry", *J. Opt. Soc. Am* (in preparation)
 Lawson P. R., 1995, *J. Opt. Soc. Am. A* 12, No. 2
 Mackay C. D., Tubbs R. N., Bell R., Burt D., Moody I., 2001, *Proc. SPIE* 4306, p. 289 in *Sensors and Cameras Systems for Scientific, Industrial, and Digital Photography Applications*
 Press W. H., Teukolsky S. A., Vetterling W. T., Flannery B. P., 1999, *Numerical Recipes in C*, 2nd edn, Cambridge University Press, Cambridge
 Traub W. A., 1990, *J. Opt. Soc. Am. A*, Vol 7, No. 9
 Shao. M, Staelin. D. H., 1977, "Long-baseline optical interferometer for astrometry", *Journal Opt. Soc. America* 67 p. 81-86.
 Thureau N., Boysen R. C., Buscher D. F., Haniff C. A., Pedretti E., Warner P. J., and Young J. S., 2002, Fringe envelope tracking at COAST. In *Interferometry for Optical Astronomy II*, volume 4838 of *Proc. SPIE*. 22-28 August 2002, Kona, Hawaii, SPIE
 Scott T. R., 1997, PhD Thesis, University of Cambridge
 Turnshek D. E., Turnshek D. A., Craine E. R., Boeshaar P. C., 1985, *An atlas of digital spectra of cool stars*, Western Research Company
 Nisenson, P. and Traub, W., 1987, "Magnitude limit of the group delay tracking method for long baseline interferometry" in *Interferometric Imaging in Astronomy*, Goad, J. ed. (National Optical Astronomy Observatories, Tuscon, Ariz.), p 129-133
 Buscher, D. F., 1989, "Low light level limits to tracking atmospheric fringe wander" in *Quantum Limited Imag-*

ing and Information Processing, 13, OSA Technical Digest Series (OSA), p. 67-69

Padilla, C. E., Karlov, V. I., Matson, L. K., Soosaar, K. and ten Brummelaar, T., 1998, "High-performance fringe tracking algorithms utilizing statistical models of atmospheric turbulence" in SPIE Astronomical Interferometry, Kona, Hawaii, 3350 p 1045-1056.

Tatarski, V. I., 1961, "Wave propagation in a turbulent medium", McGraw-Hill

This paper has been typeset from a \TeX / \LaTeX file prepared by the author.